Check for
updates

September 2017 Space-Weather Events: A Study on Magnetic Reconnection and Geoeffectiveness

Rajkumar Hajra[1] ![ORCID]

Abstract September 2017 was an extremely active space-weather period with multiple events leading to varying impacts on the Earth's magnetosphere. The geoeffectiveness of a space-weather event largely depends on the magnetic reconnection between the southward interplanetary magnetic field and the day-side northward geomagnetic field. In this work, we estimate the reconnection rates during two intense (SYM-H peak ≤ -100 nT) and two moderate (-50 nT $\geq$ SYM-H > -100 nT) geomagnetic storms, and a high-intensity long-duration continuous auroral electrojet (AE) activity (HILDCAA) event in order to assess the contribution of the reconnection to resultant geomagnetic effects. Strong reconnection rates led to intense geomagnetic storms, while moderate-intensity geomagnetic storms were associated with discrete and weaker reconnection events. Comparatively weak magnetic reconnection continuing for a long interval of time led to the HILDCAA event. On average, a significant correlation was observed between the reconnection rates and geomagnetic-activity indices. However, the relationships are found to be more complex on shorter time-scales, varying from event to event. The importance of a quantitative study of the reconnection process for the prediction of geomagnetic activity is demonstrated.

1. Introduction

Magnetic reconnection between the day-side geomagnetic field and the interplanetary magnetic field (IMF) is considered to be a dominant process for solar-wind kinetic-energy transfer into the Earth's magnetosphere (Dungey, 1961). In the day-side magnetopause current-sheet region, sufficiently strong and southward IMF can break the northward geomagnetic-field lines. The open geomagnetic-field lines connected with the IMF are

✉ R. Hajra
rajkumarhajra@yahoo.co.in

1   Indian Institute of Technology Indore, Simrol, Indore 453552, India

transported down-tail across the polar cap by the solar-wind flow, and they again reconnect at the far tail current-sheet region. Thus, the southward IMF is the most important interplanetary factor for magnetic reconnection, along with solar-wind flow speed (e.g. Tsurutani and Meng, 1972; Crooker, Feynman, and Gosling, 1977). The following are the space-weather events that are the major sources of the southward IMF: coronal mass ejections (CMEs: Illing and Hundhausen, 1986; Zurbuchen and Richardson, 2006; Lepri and Zur-buchen, 2010), solar-wind high-speed ($V_{sw} \approx 550-850$ km s^{-1}) streams (HSSs) emanating from coronal holes at the Sun (Burlaga et al., 1978; Sheeley and Harvey, 1981), and the coro-tating interaction regions (CIRs) between HSSs and low-speed ($V_{sw} \approx 300-400$ km s^{-1}) solar wind (Smith and Wolfe, 1976; Pizzo, 1985; Balogh et al., 1999; Richardson, 2018).

Solar energetic particles stored in the magnetotail through the magnetic-reconnection process precipitate in the auroral ionosphere in the form of auroral substorms (Akasofu, 1964; Ohtani, 2001; Nykyri et al., 2019). Enhancement of the ring-current particles due to strong magnetic reconnection leads to global-scale geomagnetic disturbances, commonly known as geomagnetic storms (Gonzalez et al., 1994). Discrete magnetic reconnection continuing for a long time may lead to intense auroral substorms, which can continue for several days without the occurrence of any major geomagnetic storms. These types of auroral activity have been called high-intensity long-duration continuous auroral electrojet (AE) activities (HILDCAAs) to distinguish them from nominal substorms and major geomagnetic storms (Tsurutani and Gonzalez, 1987; Hajra et al., 2013).

It is the aim of this work to quantitatively study the magnetic reconnection during geomagnetic activity. For this purpose, we choose September 2017, when a large number of space-weather events took place during a period of only one month and resulted in several geomagnetic effects such as magnetic storms (of varying intensity), substorms, and HILD-CAAs. Thus, it provided us with ample opportunity for a comparative study of magnetic reconnection during different geomagnetic disturbances. While detailed study of the space-weather events and their geomagnetic impacts during September 2017 are previously well reported (e.g. Attie et al., 2018; Berger et al., 2018; Chamberlin et al., 2018; Chertok, Belov, and Abunin, 2018; Matthiä, Meier, and Berger, 2018; O'Brien, Mazur, and Looper, 2018; Redmon et al., 2018; Schillings et al., 2018; Yan et al., 2018; Bruno et al., 2019; Jiggens et al., 2019; Piersanti et al., 2019; Werner et al., 2019; Zou et al., 2019; Scolini et al., 2020; Hajra, Tsurutani, and Lakhina, 2020, and the references therein), there is no quantitative study of the magnetic reconnection for this period. The latter is the main topic of the present work. This quantitative study is aimed at enhancing our understanding of the space-weather events and predictability of their geomagnetic impacts.

2. Data and Method of Analysis

The present work is based on the solar-wind plasma and IMF observations (one-minute temporal resolution) recorded by NASA's OMNI website (omniweb.gsfc.nasa.gov/). The OMNI database is formed by time-shifting the data collected from the *Advanced Composition Explorer* (ACE), *Wind*, and *Interplanetary Monitoring Platform 8* (IMP 8) spacecraft to the Earth's bow shock nose. The IMF data in the geocentric solar magnetospheric (GSM) coordinate system are used in this work. These data are utilized to identify and characterize the interplanetary events.

For detailed analyses of the interplanetary discontinuities and events during September 2017, we refer the reader to Hajra, Tsurutani, and Lakhina (2020). However, here we mention the definitions for the same quantities, used in the present work. Interplanetary

discontinuities characterized by abrupt increases in the solar-wind plasma speed [V_{sw}], density [N_{sw}], ram pressure [P_{sw}], temperature [T_{sw}], and IMF magnitude [B_0] are defined as fast forward shocks (FSs) when the estimated magnetosonic Mach number (MMN) > 1. Discontinuities with MMN < 1 are defined as waves. Reverse waves (RWs) are the discontinuities with abrupt increase in V_{sw} accompanied by decreases in N_{sw}, P_{sw}, T_{sw}, and IMF B_0 when MMN < 1. Turbulent plasma and IMF followed by FSs are identified as interplanetary sheaths (Kennel, Edmiston, and Hada, 1985; Tsurutani and Lin, 1985; Tsurutani et al., 1988). It should be noted that the fast interplanetary CMEs (ICMEs) propagating faster than the local upstream magnetosonic speed generate interplanetary shocks followed by sheaths (see Kennel, Edmiston, and Hada, 1985; Tsurutani et al., 1988). A subset of ICMEs is called magnetic clouds (MCs): these are identified by low plasma-β [the ratio of plasma pressure to magnetic pressure] and low plasma temperature [T_{sw}] (Burlaga et al., 1981; Klein and Burlaga, 1982; Tsurutani and Gonzalez, 1997). The solar-coronal-hole-emanated HSSs are identified at the Earth's bow shock with the peak V_{sw} between ≈ 550 and ≈ 850 km s^{-1}. These are preceded by CIRs characterized by the compressed plasma and IMF.

Using the solar-wind plasma and IMF variation, we estimated the magnetic-reconnection parameters. The reconnection electric field or the magnetic-flux transfer rate is expressed as VB_s, where V is V_{sw}, $B_s = \mathrm{abs}(B_z)$ when IMF $B_z < 0$, and $B_s = 0$ when $B_z \geq 0$. VB_s has been shown to be the main driver of geomagnetic activity (e.g. Burton, McPherron, and Russell, 1975; Tsurutani et al., 1992; Finch, Lockwood, and Rouillard, 2008). We estimated the Akasofu ϵ-parameter [$V_{sw}B_0^2 \sin^4(\theta/2) R_{CF}^2$], which gives an approximate measure of the magnetospheric energy input rate (Perreault and Akasofu, 1978). Here θ is the IMF orientation clock angle, and R_{CF} is the Chapman–Ferraro magnetopause distance (Chapman and Ferraro, 1931; Shue and Chao, 2013). More recently Milan, Gosling, and Hubert (2012) developed a parameter to quantify the reconnection rate [ϕ_D] in terms of the magnetic-flux transport across the day-side magnetopause:

$$\phi_D = L_{\mathrm{eff}} V_{sw} B_{yz} \, \sin^{\frac{9}{2}}(\frac{\theta}{2}),$$ (1)

where $B_{yz} = (B_y^2 + B_z^2)^{1/2}$ and L_{eff} is an effective length scale given by

$$L_{\mathrm{eff}} = 3.8 \mathrm{R}_\oplus (\frac{V_{sw}}{400})^{\frac{1}{3}},$$ (2)

where $\mathrm{R}_\oplus$ is the Earth's radius. The location of the day-side magnetopause [R_{MP}] was estimated from the pressure balance between the solar-wind dynamic pressure and the Earth's magnetic pressure as follows:

$$R_{MP} = R_\oplus (\frac{2B_E^2}{\mu_0 \mathrm{m}_p N_{sw} V_{sw}^2})^{\frac{1}{6}},$$ (3)

where B_E is the equatorial magnetic field on the Earth's surface, μ_0 is the free space permeability, and m_p is the solar-wind proton mass.

The geomagnetic activities are studied by the symmetric ring-current SYM-H index (Iyemori et al., 2010) and the auroral SME and SML indices (Gjerloev, 2009). The SYM-H index data (one-minute temporal resolution) are obtained from the World Data Center for Geomagnetism, Kyoto, Japan (wdc.kugi.kyoto-u.ac.jp/). The auroral indices (one-minute temporal resolution) are taken from the SuperMAG network (supermag.jhuapl.edu/). Based on the SYM-H peak, the magnetic storms are defined as moderate (-50 nT $\geq$ SYM-H peak

Table 1 Details of the geomagnetic storms and the HILDCAA event under study[a].

Event	Main phase onset[b] [UT]	Recovery phase onset[b] [UT]	End of recovery phase[b] [UT]	SYM-H peak [nT]	SME peak [nT]
IMS_07	07 Sep. 20:12	08 Sep. 01:10	08 Sep. 11:20	−146	4464
IMS_08	08 Sep. 11:26	08 Sep. 13:56	09 Sep. 06:44	−115	4330
MMS_12	12 Sep. 22:05	13 Sep. 00:12	13 Sep. 01:37	−65	1856
HILDCAA_14[b]	14 Sep. 14:01		17 Sep. 17:26	−44	1749
MMS_27	27 Sep. 19:06	28 Sep. 05:57	29 Sep. 07:52	−74	2683

[a]The identifications are based on Hajra, Tsurutani, and Lakhina (2020).

[b]For the HILDCAA event, the main-phase onset and the end of recovery-phase stand for the start and end times, and it does not have a recovery-phase onset.

> -100 nT), intense (-100 nT $\geq$ SYM-H peak > -250 nT), and super (SYM-H peak ≤ -250 nT) storms (Gonzalez et al., 1994). An auroral substorm is defined and identified (Newell and Gjerloev, 2011) as an interval of a sharp decrease in the SML index. This is followed by the recovery to the pre-substorm values. Super-substorms (SSSs) are extremely intense substorms. They are defined by the peak SML < -2500 nT, a threshold used previously by Tsurutani et al. (2015) and Hajra et al. (2016). Based on Tsurutani and Gonzalez (1987), HILDCAAs are identified as intervals of i) high-intensity (the peak AE > 1000 nT), ii) long-duration ($>$ two days), iii) continuous (no AE < 200 nT for two hours or more at a time) AE activity, iv) occurring during a non-storm condition (with SYM-H > -50 nT) or during a storm recovery phase. While the original definition of HILDCAAs involves the AE index, we have substituted the SME index for the AE index in this work. The AE index is based on the geomagnetic field observations from 12 stations located around $60° - 70°$ N (geomagnetic) latitude (Davis and Sugiura, 1966). Thus it is not suitable to study any auroral effects at very high and/or very low latitudes. This insufficiency can be overcome by the use of the SME index that is based on the SuperMAG network of ≈ 300 ground-magnetometer measurements. This network has a wider (latitude and longitude) coverage than the AE sites.

3. Results

3.1. Geomagnetic Activity During September 2017: An Overview

Figure 1 shows the solar-wind plasma and IMF variations and the resultant geomagnetic impacts during the month of September 2017. From the variations of the geomagnetic SME, SML, and SYM-H indices, two intense and two moderate geomagnetic storms, two SSSs, and a HILDCAA event were identified. The details of the magnetic storms and the HILD-CAA are listed in Table 1. From the variations of the solar-wind plasma V_{sw}, N_{sw}, P_{sw}, T_{sw}, β, the IMF magnitude [B_0], and the components B_x, B_y, and B_z, the interval of the study is found to be characterized by multiple space-weather events. We have marked the major interplanetary discontinuities and interplanetary events associated with the above-mentioned geomagnetic activities only. For a complete/detailed list and analyses of interplanetary and geomagnetic events, we refer the reader to Hajra, Tsurutani, and Lakhina (2020).

The solar-wind plasma and IMF led to large variations in the day-side magnetopause location [R_{MP}], and solar-wind–magnetosphere coupling and reconnection rates given by
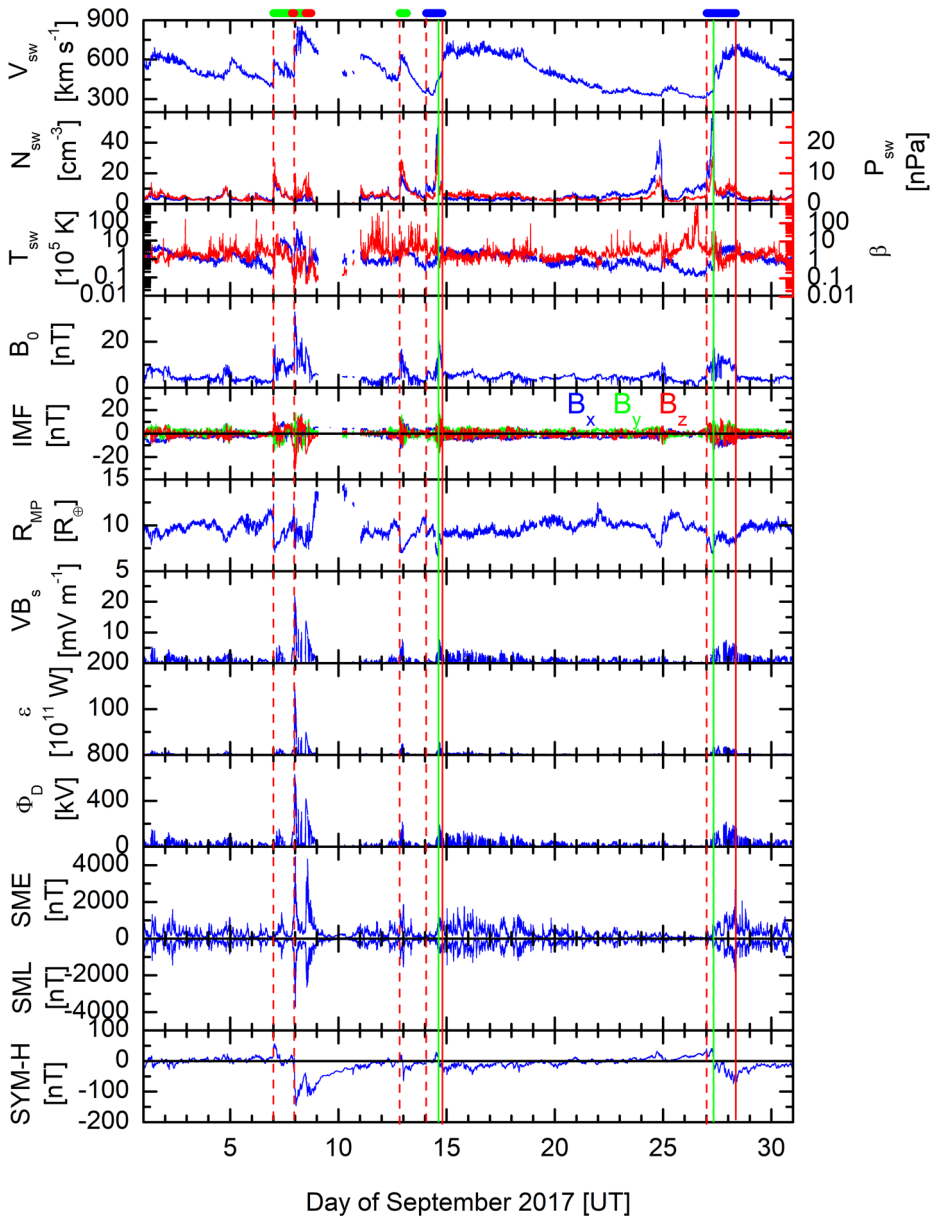
Figure 1 Solar-wind/interplanetary and geomagnetic variations during September 2017. From top to bottom, the panels show the solar-wind plasma speed [V_{sw}], plasma density [N_{sw}] (blue, legend on the left), and ram pressure [P_{sw}] (red, legend on the right) in the same panel, temperature [T_{sw}] (blue, legend on the left), and plasma-β (red, legend on the right) in the same panel, IMF B_0, B_x (blue), B_y (green), and B_z (red) components in the same panel, day-side magnetopause distance [R_{MP}], reconnection parameters [VB_s, ϵ, ϕ_D], geomagnetic SME, SML, and SYM-H indices, respectively. The temporal resolution of the data is one minute. Vertical lines indicate fast forward shocks (FSs, red-dashed lines), reverse waves (RWs, red-solid lines), and stream interfaces (SIs, green-solid lines). Horizontal bars at the top indicate interplanetary sheaths (Sh, green), magnetic clouds (MCs, red), and CIRs (blue).

VB_s, ϵ, and ϕ_D. In the following sections, a detailed study on R_{MP}, VB_s, ϵ, and ϕ_D during the geomagnetic events is presented. Relationships of these parameters with the associated geomagnetic disturbances will be assessed.

3.2. Intense Geomagnetic Storms During 7 – 8 September 2017

The solar-wind/interplanetary variations during 6 – 10 September (Figure 2) show a complex interplanetary interval starting with a fast forward shock (FS_07_1, vertical red-dashed line) at $\approx$ 00:00 UT on 7 September. This is characterized by abrupt increases in V_{sw} (from $\approx$ 391 to $\approx$ 591 km s^{-1}), N_{sw} (from $\approx$ 4 to $\approx$ 14 cm^{-3}), P_{sw} (from $\approx$ 2 to $\approx$ 9 nPa), T_{sw} (from $\approx 0.3 \times 10^5$ to $\approx 1.8 \times 10^5$ K), and B_0 (from $\approx$ 4 to $\approx$ 13 nT). The 4.5-times P_{sw} increase at the shock compressed the magnetosphere inward, from $\approx$ 10.9 to $\approx$ 7.7 R$_\oplus$.

FS_07_1 is followed by an interplanetary sheath (Sh_07_1, horizontal green bar) identified by turbulent plasma and IMF, from $\approx$ 00:00 UT to $\approx$ 20:24 UT on 7 September. At the trailing end of the sheath, a magnetic cloud (MC_07, horizontal red bar) is detected as a region of low plasma-β ($\approx$ 0.04) and low T_{sw} ($\approx 0.2 \times 10^5$ K) from $\approx$ 20:24 UT to $\approx$ 23:02 UT on 7 September. It is worth mentioning that during the MC, the IMF had a stable southward component, without any field rotation as one would expect during the classical flux rope structure of a MC. The MC provided a southward IMF with peak B_z-component of ≈ -10 nT. This southward IMF caused increases in the reconnection electric field [VB_s] to $\approx$ 4.9 mV m^{-1}, magnetospheric energy input rate [ϵ] to $\approx 10.4 \times 10^{11}$ W, and reconnection rate [ϕ_D] to $\approx$ 129.7 kV. The enhanced magnetic-reconnection rate led to the onset of an intense magnetic storm (IMS_07) at $\approx$ 20:12 UT on 7 September (Table 1). The IMS_07 onset can be identified by the southward turning of the SYM-H index attaining a peak value of -29 nT at $\approx$ 22:48 UT on 7 September. Thus the main phase onset and the first step decrease in the SYM-H index can be attributed to the sheath (Sh_07_1)–MC (MC_07) interaction.

MC_07 was superposed by another fast forward shock (FS_07_2, vertical red-dashed line) at $\approx$ 23:02 UT on 7 September that compressed the magnetosphere to $\approx$ 8.2 R$_\oplus$. FS_07_2 was characterized by increases in V_{sw} (from $\approx$ 477 to $\approx$ 708 km s^{-1}), N_{sw} (from $\approx$ 3 to $\approx$ 9 cm^{-3}), P_{sw} (from $\approx$ 1 to $\approx$ 6 nPa), T_{sw} (from $\approx 0.2 \times 10^5$ to $\approx 5.8 \times 10^5$ K), and IMF B_0 (from $\approx$ 10 to $\approx$ 25 nT). This MC–shock interaction resulted in a turbulent sheath (Sh_07_2, horizontal green bar) from $\approx$ 23:02 UT on 7 September to $\approx$ 11:31 UT on 8 September with a stronger southward IMF B_z peak of ≈ -31 nT. The latter led to a large magnetic-flux flow indicated by peak VB_s of $\approx$ 21.7 mV m^{-1}, peak $\epsilon \approx 149.0 \times 10^{11}$ W, and enhanced $\phi_D \approx$ 630.9 kV. The enhanced reconnection rate resulted in a second step decrease in the SYM-H index to -93 nT at $\approx$ 23:33 UT on 7 September. This was followed by a third step decrease in SYM-H to -146 nT at $\approx$ 01:10 UT on 8 September. The storm peak was associated with a large magnetospheric compression to $\approx$ 7.4 R$_\oplus$. During the main phase of IMS_07 a supersubstorm (SSS_07), with the SML and SME intensities of -3712 nT and 4464 nT, respectively at $\approx$ 00:24 UT on 8 September, was detected.

Sh_07_2 was followed by a magnetic cloud (MC_08, horizontal red bar) from $\approx$ 11:31 UT to $\approx$ 18:00 UT on 8 September. This is characterized by a low plasma-β ($\approx$ 0.05), a low T_{sw} ($\approx 0.2 \times 10^5$ K), and a smooth IMF B_z south-to-northward rotation. The southward component with peak B_z of ≈ -17 nT resulted in the second intense magnetic storm (IMS_08) (Table 1). IMS_08 started at $\approx$ 11:26 UT and attained the peak SYM-H intensity of -115 nT at $\approx$ 13:56 UT on 8 September. The storm interval was characterized by large VB_s ($\approx$ 13.8 mV m^{-1}), ϵ ($\approx 49.4 \times 10^{11}$ W), ϕ_D ($\approx$ 417.9 kV), and peak magnetospheric compression to $\approx$ 7.8 R$_\oplus$. Another SSS (SSS_08), characterized by SML and SME
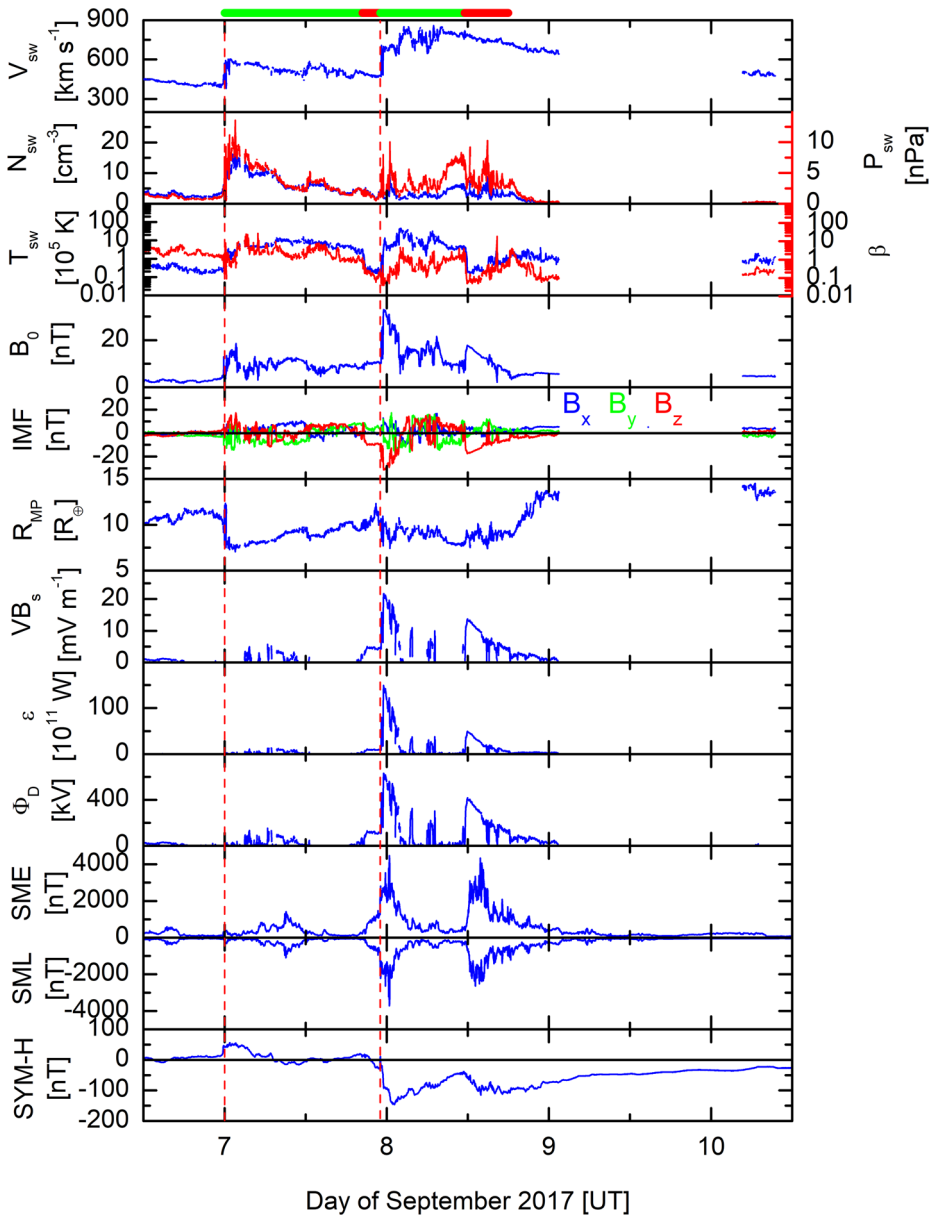
Figure 2 Intense geomagnetic storms during 7–8 September 2017. The panels are in the same format as in Figure 1. The vertical red-dashed lines indicate the fast forward shocks FS_07_1 and FS_07_2, respectively. The horizontal green bars indicate the sheaths Sh_07_1 and Sh_07_2, respectively. The horizontal red bars indicate the magnetic clouds MC_07 and MC_08, respectively.

intensities of −2642 nT and 4330 nT, respectively at ≈ 13:08 UT was detected during the IMS_08 main phase. During the storm recovery phase a large relaxation of magnetopause to ≈ 13.7 $R_\oplus$ can be noted (at ≈ 23:35 UT on 8 September).
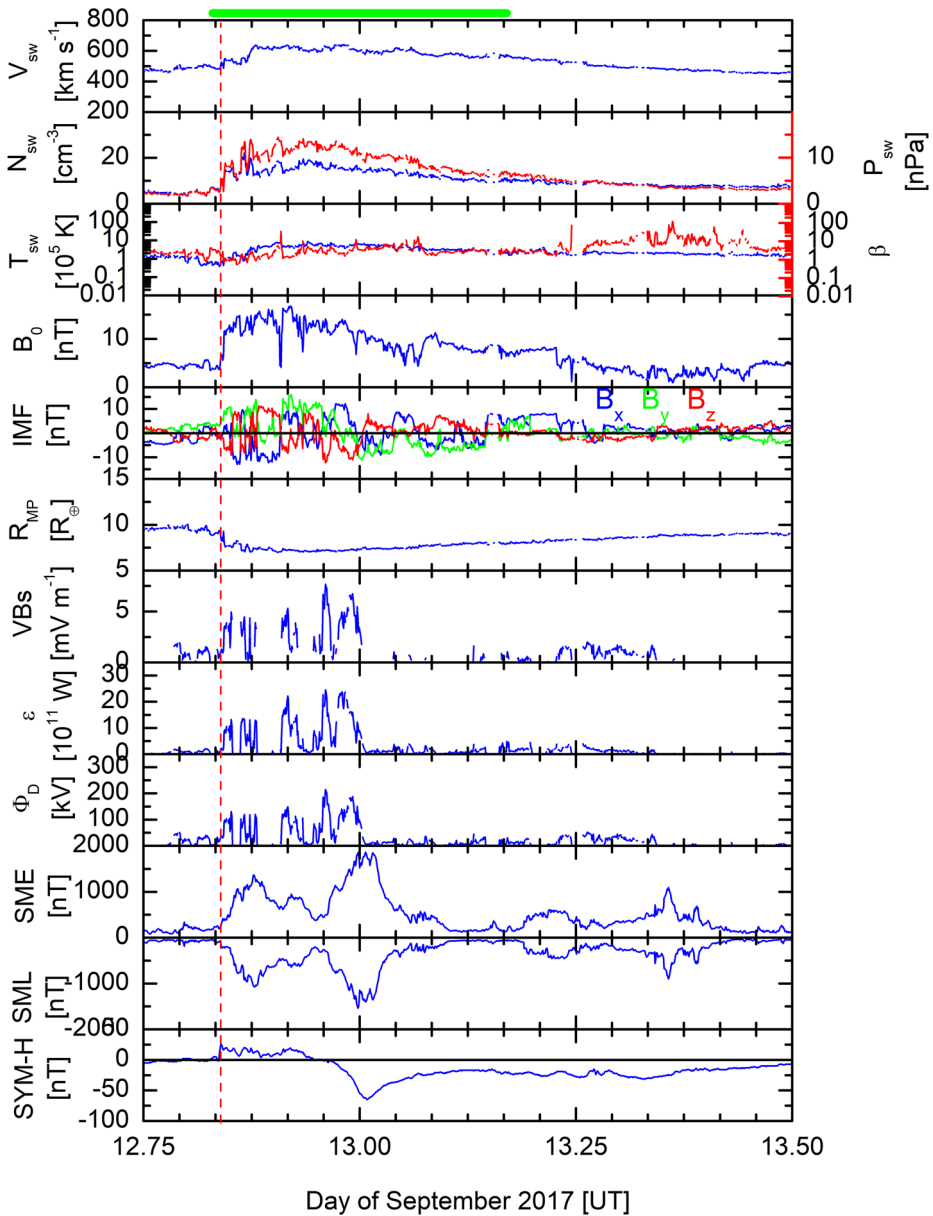
Figure 3   Moderate geomagnetic storm during 12–13 September 2017. The panels are in the same format as in Figure 1. The vertical red-dashed line indicates the fast forward shock FS_12. The horizontal green bar indicates the sheath Sh_12.

3.3. Moderate Geomagnetic Storm During 12–13 September 2017

Figure 3 shows interplanetary variations leading to a moderate magnetic storm (MMS_12) (Table 1). A fast forward shock (FS_12, vertical red-dashed line) was incident on the magnetosphere at ≈ 19:55 UT on 12 September. This was characterized by abrupt increases in V_{sw}

from ≈ 482 to ≈ 536 km s^{-1}, in N_{sw} from ≈ 6 to ≈ 14 cm^{-3}, in P_{sw} from ≈ 3 to ≈ 10 nPa, in T_{sw} from $\approx 0.4 \times 10^5$ to $\approx 0.9 \times 10^5$ K, and in IMF B_0 from ≈ 4 to ≈ 11 nT. A sheath (Sh_12, horizontal green bar) followed the shock, from $\approx 19{:}55$ UT on 12 September to $\approx 04{:}05$ UT on 13 September. Sh_12 was characterized by largely fluctuating plasma and IMF. However, it should be mentioned that the sheath was unusual in that it was not followed by any typical ICME signature such as a MC (see Hajra, Tsurutani, and Lakhina, 2020, for a detailed discussion of the cause, which is beyond the scope of the present work). Thus, the sheath trailing end was determined approximately by the decrease in the IMF fluctuation amplitude.

Following the shock (FS_12), the magnetopause was gradually compressed inward from ≈ 9.3 to ≈ 7.0 R$_\oplus$ during the sheath (Sh_12). This interval is characterized by discrete southward IMF B_z-components. It led to largely fluctuating magnetic-flux flow (as indicated by VB_s with a peak of ≈ 7.7 mV m^{-1}), magnetospheric energy input rate (ϵ peak $\approx 24.5 \times 10^{11}$ W), and magnetic-reconnection rate (ϕ_D peak ≈ 214.5 kV). They resulted in MMS_12 with the peak SYM-H intensity of -65 nT at $\approx 00{:}12$ UT on 13 September. The magnetopause relaxed gradually and returned to ≈ 9.0 R$_\oplus$ during the storm-recovery phase.

3.4. HILDCAA During 14 – 17 September 2017

A long-duration intense auroral activity or HILDCAA (Table 1) is recorded from $\approx 14{:}01$ UT on 14 September to $\approx 17{:}26$ UT on 17 September, as can be observed from the auroral SME and SML indices (Figure 4). The variation of SYM-H shows that while there were two intervals with enhanced and fluctuating ring-current activity, there was no major geomagnetic storm during the interval (peak SYM-H was only ≈ -44 nT). The interplanetary variation shows a CIR (CIR_14, horizontal blue bar) around the HILDCAA onset, followed by a solar-wind HSS (HSS_14) during the HILDCAA interval.

The CIR_14 leading and trailing edges are characterized by a fast forward shock FS_14 (vertical red-dashed line) at $\approx 01{:}26$ UT on 14 September and a reverse wave RW_14 (vertical red solid line) at $\approx 19{:}26$ UT on 14 September, respectively. While FS_14 is characterized by increases in V_{sw} (from ≈ 343 to ≈ 373 km s^{-1}), N_{sw} (from ≈ 5 to ≈ 13 cm^{-3}), P_{sw} (from ≈ 1 to ≈ 4 nPa), T_{sw} (from $\approx 0.3 \times 10^5$ to $\approx 1.0 \times 10^5$ K), and IMF B_0 (from ≈ 3 to ≈ 5 nT), RW_14 is characterized by increase in V_{sw} (from ≈ 516 to ≈ 576 km s^{-1}) accompanied by simultaneous decreases in N_{sw} (from ≈ 8 to ≈ 4 cm^{-3}), P_{sw} (from ≈ 5 to ≈ 3 nPa), T_{sw} (from $\approx 4.1 \times 10^5$ to $\approx 2.4 \times 10^5$ K), and IMF B_0 (from ≈ 12 to ≈ 8 nT). A stream interface (SI_14, vertical green-solid line) is observed at $\approx 15{:}07$ UT on 14 September, when N_{sw} decreased from ≈ 43 to ≈ 7 cm^{-3}, T_{sw} increased simultaneously from $\approx 1.0 \times 10^5$ to $\approx 5.4 \times 10^5$ K accompanied by a slow increase in V_{sw} from ≈ 445 to ≈ 458 km s^{-1}. HSS_14 following CIR_14 is characterized by the peak V_{sw} of ≈ 730 km s^{-1} and an interplanetary Alfvén-wave train as evident from the fluctuating IMF B_z-component.

The fast forward shock FS_14 compressed the magnetopause from ≈ 11.2 to ≈ 8.7 R$_\oplus$, which was followed by a further compression to ≈ 6.5 R$_\oplus$ by the pressure pulse preceding SI_14. The most interesting feature of the HILDCAA is that the entire HILDCAA interval is characterized by enhanced and fluctuating magnetic-flux transfer (VB_s peak ≈ 3.9 mV m^{-1}), magnetospheric energy input (ϵ peak $\approx 5.0 \times 10^{11}$ W), and magnetic-reconnection rate (ϕ_D peak ≈ 120 kV). However, as evident from the R_{MP} variation, the magnetopause was much relaxed and away from the Earth (≈ 9.5 R$_\oplus$) as compared to during the geomagnetic storms.
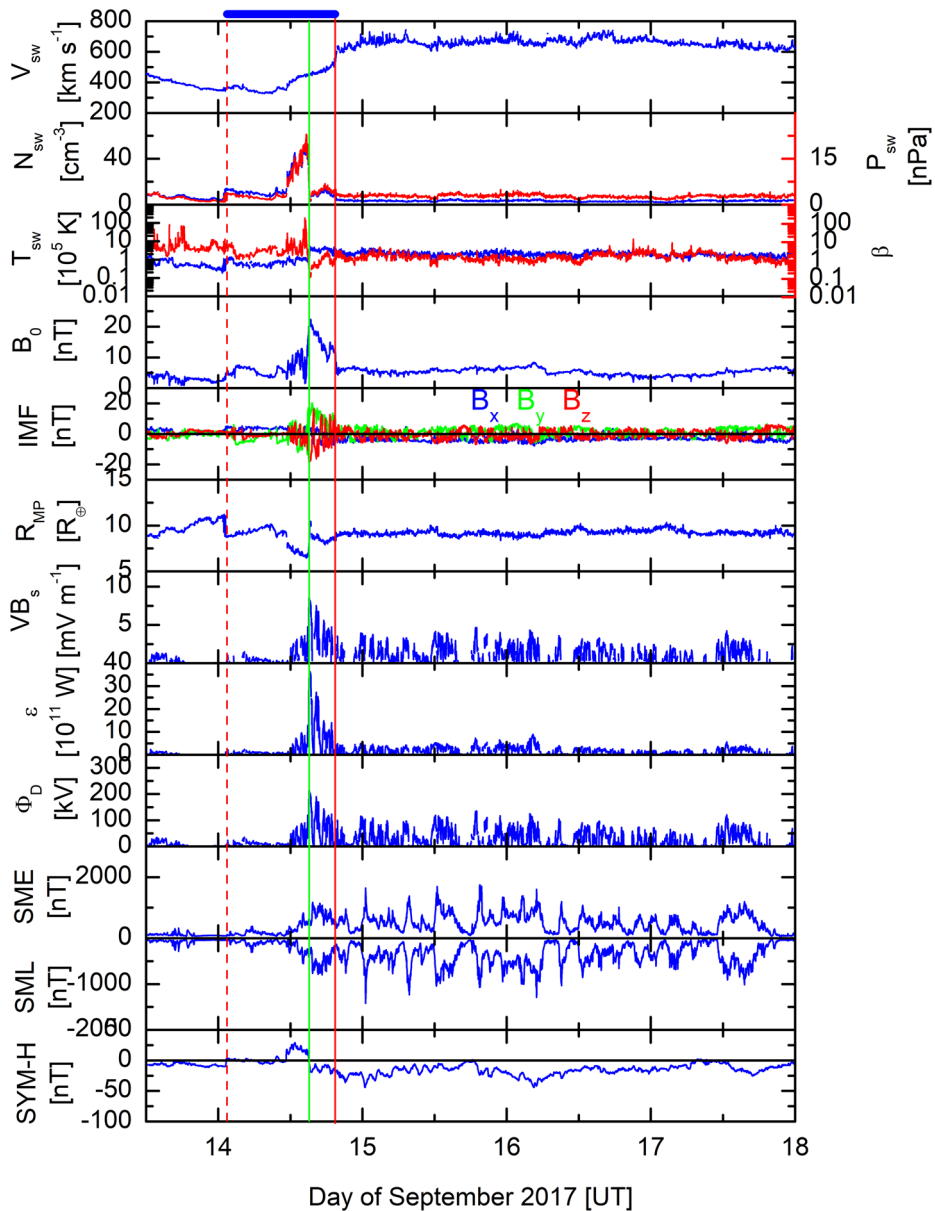
Figure 4 HILDCAA during 14–17 September 2017. The panels are in the same format as in Figure 1. The vertical red-dashed line indicates the fast forward shock FS_14, the vertical green-solid line indicates the stream interface SI_14, and the vertical red-solid line indicates the reverse wave RW_14. The horizontal blue bar indicates CIR_14.

3.5. Moderate Geomagnetic Storm During 27–28 September 2017

Figure 5 shows interplanetary events leading to a moderate magnetic storm (MMS_27) during 27–28 September (Table 1). A CIR (CIR_27, horizontal blue bar) is observed from
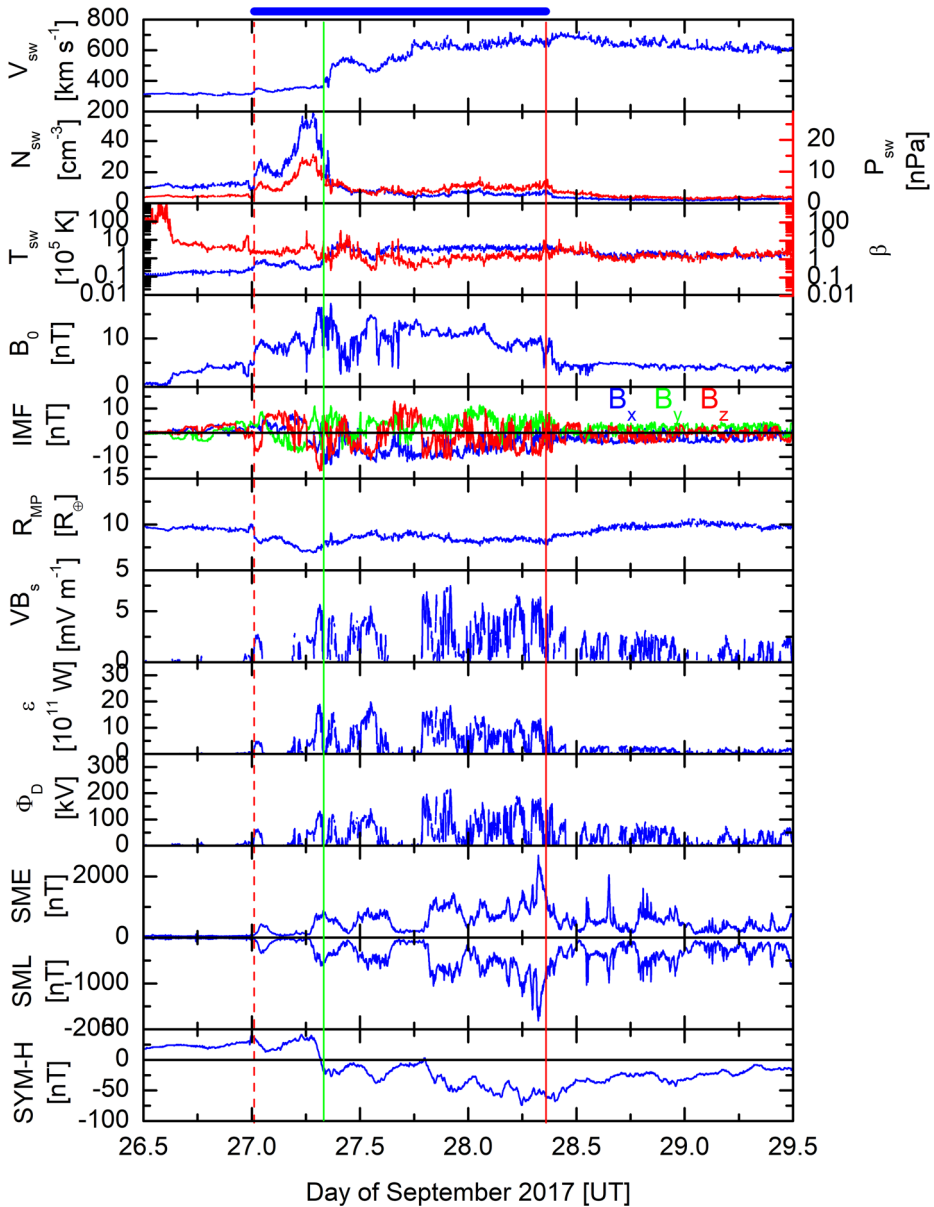
Figure 5 Moderate geomagnetic storm during 27–28 September 2017. The panels are in the same format as in Figure 1. The vertical red-dashed line indicates the fast forward shock FS_27, the vertical green-solid line indicates the stream interface SI_27, the vertical red-solid line indicates the reverse wave RW_28. The horizontal blue bar indicates CIR_27.

$\approx$ 00:15 UT on 27 September to $\approx$ 08:38 UT on 28 September between a solar-wind low-speed stream with V_{sw} of $\approx$ 325 km s^{-1} and a HSS (HSS_28) with V_{sw} of $\approx$ 720 km s^{-1}. The CIR is bounded by a fast forward shock (FS_27, vertical red-dashed line) at the leading edge and a reverse wave (RW_28, vertical red-solid line) at the trailing edge. A stream interface
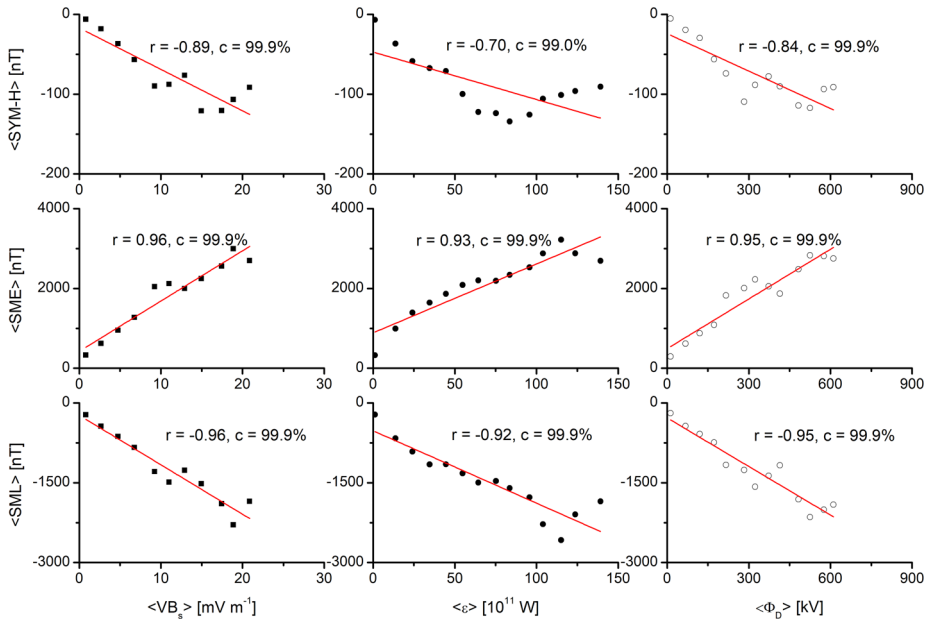
Figure 6 Average geomagnetic activity vs. magnetic reconnection. From top to bottom, the panels show the variations of the average geomagnetic SYM-H, SME, and SML indices with the average VB_s (left panel), ϵ (middle panel), and ϕ_D (right panel), respectively. The linear regression lines, regression coefficients [r], and confidence levels [c] of the statistical analysis are shown in each panel.

(SI_27, vertical green-solid line) is observed at $\approx$ 07:58 UT on 27 September that is characterized by a N_{sw} decrease from $\approx$ 44 to $\approx$ 19 cm^{-3} and a T_{sw} increase from $\approx 0.4 \times 10^5$ to $\approx 1.7 \times 10^5$ K with a slow increase in V_{sw} from $\approx$ 358 to $\approx$ 420 km s^{-1}.

Following the shock FS_27, the magnetosphere was compressed from $\approx$ 9.9 to $\approx$ 6.9 R$_\oplus$ during CIR_27. IMF B_z was largely fluctuating. Discrete southward components of the IMF led to largely fluctuating magnetic-flux flow (VB_s peak $\approx$ 7.5 mV m^{-1}), magnetospheric energy input (ϵ peak $\approx 19.8 \times 10^{11}$ W), and magnetic-reconnection rate [ϕ_D] peak $\approx$ 214.4 kV) resulting in a gradually developing storm main phase (MMS_27) with the peak SYM-H intensity of -74 nT at $\approx$ 05:57 UT on 28 September. During the MMS_27 peak the magnetosphere was compressed to $\approx$ 7.7 R$_\oplus$, and it relaxed to $\approx$ 10.0 R$_\oplus$ after the recovery. Interestingly, an enhanced reconnection rate can be observed during the storm-recovery phase as well.

3.6. Geomagnetic Activity vs. Magnetic Reconnection

For the entire period of the study, from 1 to 30 September, we estimated the magnetic-flux flow [VB_s], magnetospheric-energy input rate [ϵ] and magnetic-reconnection rate [ϕ_D] at the Earth's magnetospheric bow shock (see Figure 1). To study the average dependence of the geomagnetic activity (depicted by the SYM-H, SME, and SML indices) on these parameters, the entire data set was binned into different values of average VB_s [$\langle VB_s \rangle$], average ϵ [$\langle \epsilon \rangle$], and average ϕ_D [$\langle \phi_D \rangle$]. The average values of the SYM-H, SME, and SML indices were estimated for each bin. The result is shown in Figure 6.

From the high correlation coefficients ($|r| = 0.70 - 0.96$), it can be concluded that the variations of the geomagnetic activity are strongly associated with (correlated or anti-
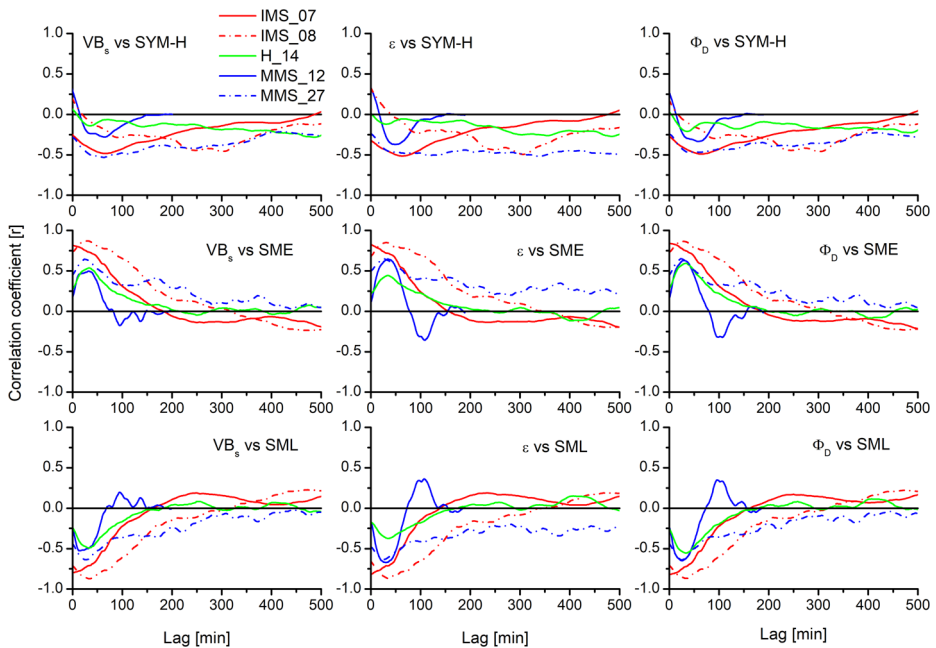
Figure 7 Time-lagged cross-correlation analysis between the geomagnetic indices and the reconnection parameters during the geomagnetic events under study.

correlated to) the VB_s, ϵ, and ϕ_D parameters. The relationships are statistically significant at $> 99\%$ confidence $[c]$ level (Student's t-test; Student, 1908). It may be noted that, for obvious reasons, the westward (negative) ring-current index SYM-H, and westward (negative) auroral electrojet index SML exhibit anti-correlation (negative) with the reconnection parameters, while the auroral electrojet index SME (positive quantity) exhibits correlation (positive) with the reconnection parameters.

From Figure 6, the SYM-H ring-current index is found to exhibit weaker association with the reconnection parameters, compared to the auroral indices SME and SML. This result indicates different growth and loss mechanisms of ring-current and auroral ionospheric currents. To have a better understanding of auroral ionospheric and ring currents during different geomagnetic events, the time-lagged cross-correlation analyses (Davis, 2002) are performed separately for the events. The time lags of the geomagnetic indices from the reconnection parameters are increased from zero, and corresponding correlation coefficients $[r]$ are estimated. The results are shown in Figure 7. The figure clearly shows the time-varying relationships between the geomagnetic indices and the reconnection parameters, and how they vary during different geomagnetic events. The peak correlation coefficients and corresponding time lags (in minutes) are listed in Table 2.

Consistent with Figure 6, the SYM-H index exhibits a weaker association/anti-correlation ($r = -0.23$ to -0.53) with the reconnection parameters compared to the SME ($r = 0.44$ to 0.87) and SML ($r = -0.38$ to -0.87) indices during any geomagnetic event (Figure 7, Table 2). During any particular event, the SYM-H index exhibited better association with the ϵ-parameter than with VB_s and ϕ_D. The SYM-H relationships are the worst during the HILDCAA event ($r = -0.23$ to -0.30), they are sometimes comparable ($r = -0.28$ to -0.53) during the moderate storms (MMS_12 and MMS_27). Another important feature of

Table 2 Time-lagged cross-correlation analysis[a] during the geomagnetic events under study.

	IMS_07	IMS_08	MMS_12	HILDCAA_14	MMS_27
VB_s–SYM-H	−0.48 (66)	−0.46 (305)	−0.28 (64)	−0.28 (485)	−0.53 (63)
VB_s–SME	0.81 (1)	0.87 (29)	0.50 (32)	0.54 (34)	0.64 (25)
VB_s–SML	−0.80 (0)	−0.87 (34)	−0.53 (15)	−0.49 (33)	−0.64 (28)
ϵ–SYM-H	−0.52 (63)	−0.49 (306)	−0.37 (50)	−0.30 (563)	−0.52 (339)
ϵ–SME	0.82 (0)	0.85 (31)	0.65 (34)	0.44 (35)	0.65 (26)
ϵ–SML	−0.82 (0)	−0.87 (36)	−0.67 (31)	−0.38 (36)	−0.64 (26)
ϕ_D–SYM-H	−0.49 (65)	−0.46 (306)	−0.33 (0.59)	−0.23 (484)	−0.47 (42)
ϕ_D–SME	0.84 (0)	0.86 (29)	0.63 (31)	0.59 (33)	0.65 (24)
ϕ_D–SML	−0.82 (0)	−0.87 (34)	−0.65 (26)	−0.55 (34)	−0.64 (25)

[a]The values in the table represent the peak cross-correlation coefficients [r] and the corresponding time lags in minutes (in parentheses) between the geomagnetic indices and the coupling functions.

the SYM-H relationships is that they peak at some time lag, varying from ≈ 42 to 563 minutes, from the coupling parameters.

Both SME and SML exhibited the highest associations with the coupling parameters during the intense magnetic storm IMS_08. The associations are significantly higher than during the intense storm IMS_07. Interestingly, while the relationships of the auroral indices with the coupling functions peak at $\approx 0 - 1$-minute lags during IMS_07, they peak at $\approx 29 - 36$-minute lags during IMS_08. As discussed in Section 3.2 (Figure 2), IMS_07 was followed by IMS_08 and they resulted from a complex interplay between various space-weather events such as fast forward shocks, sheaths, and MCs. Thus, larger correlations during IMS_08 compared to during IMS_07 may result from the fact that the magnetosphere was already energized when IMS_08 started.

Overall, the relationships of the auroral electrojet indices with the coupling functions are weaker during the moderate storms and the HILDCAA event compared to during the intense storms. They peak at time lags of $\approx 15 - 36$ minutes from the coupling functions. The time lags are significantly shorter than the time lags of the SYM-H index from the coupling functions.

4. Summary and Discussion

We studied the impacts of the solar-wind/interplanetary variations on the magnetopause position [R_{MP}], magnetic-flux transfer [VB_s], magnetospheric-energy input rate [ϵ], and magnetic-reconnection rate [ϕ_D] during two intense and two moderate geomagnetic storms, and a HILDCAA event. The main results are summarized in Table 3.

The reconnection parameters [VB_s, ϵ, and ϕ_D] were quite large and exhibited sharp variations during the main phases of the intense magnetic storms, compared to those during the moderate storm main phases and the HILDCAA event when the parameters were largely fluctuating and had smaller peaks. The main factors controlling the geomagnetic activity during the interplanetary events are the magnetic-flux transfer, magnetospheric-energy input rate, and magnetic-reconnection rate. These are largely controlled by the intensity and orientation of the IMF through the process of magnetic reconnection between the IMF and the day-side magnetopause (geomagnetic) field. The present work clearly demonstrates the

Table 3 Details of the magnetic-reconnection characteristics during the geomagnetic events under study.

Event	SYM-H peak [nT]	SME peak [nT]	VB_s peak [mV m^{-1}]	ϵ peak [10^{11} W]	ϕ_D peak [kV]	R_{MP} peak [$R_\oplus$]
IMS_07	−146	4464	21.7	149.0	630.9	7.4
IMS_08	−115	4330	13.8	49.4	417.9	7.8
MMS_12	−65	1856	7.7	24.5	214.5	7.0
HILDCAA_14	−44	1749	3.9	5.0	120.0	9.5
MMS_27	−74	2683	7.5	19.8	214.4	7.7

importance of the large-amplitude reconnection rate for intense geomagnetic storms. On the other hand, the discrete reconnection rate leads to only moderate-intensity geomagnetic storms. Comparatively weak magnetic reconnection continuing for a long interval of time can lead to HILDCAA events. The location of the day-side magnetopause, which depends on the pressure balance between the solar-wind ram pressure and the magnetospheric magnetic pressure, exhibited large variability during the geomagnetic activity. These results are consistent with present understanding of geomagnetic activity (Tsurutani and Gonzalez, 1987; Tsurutani et al., 1988, 1995, 2006; Gonzalez et al., 1994; Zhang et al., 2007; Echer, Gonzalez, and Tsurutani, 2008; Hajra et al., 2014; Meng, Tsurutani, and Mannucci, 2019; Hajra, Tsurutani, and Lakhina, 2020; Tsurutani and Hajra, 2021).

On the average, the intensity of the ring-current index and the auroral-activity indices exhibited linear relationships with the reconnection parameters. However, short-term variations of the geomagnetic indices exhibited more complex relationships with the reconnection parameters, and they are strongly dependent on the geomagnetic events. During any geomagnetic event, the reconnection parameters have the weakest control on the ring-current index compared to the auroral electrojet currents. In addition, ring currents exhibit significant time-lagged variations with respect to the reconnection parameters. This is a new finding, and the complex, nonlinear relationship of the ring currents with the magnetic reconnection requires further investigation.

Weak relationships of the auroral indices with the reconnection parameters during the moderate storms and the HILDCAA event indicate the challenges of predicting weak storms and HILDCAAs. On the other hand, intense storms with distinguished and obvious solar/interplanetary drivers exhibit better predictability.

A more detailed and quantitative understanding of the magnetic reconnection leading to the geomagnetic activity is required for augmenting the prediction capability. This can be obtained from further case studies involving large number of space-weather events.

References

Akasofu, S.-I.: 1964, The development of the auroral substorm. *Planet. Space Sci.* **12**, 273. DOI.

Attie, R., Kirk, M.S., Thompson, B.J., Muglach, K., Norton, A.A.: 2018, Precursors of magnetic flux emergence in the moat flows of active region AR12673. *Space Weather* **16**, 1143. DOI.

Balogh, A., Bothmer, V., Crooker, N.U., Forsyth, R.J., Gloeckler, G., Hewish, A., Hilchenbach, M., Kallenbach, R., Klecker, B., Linker, J.A., Lucek, E., Mann, G., Marsch, E., Posner, A., Richardson, I.G., Schmidt, J.M., Scholer, M., Wang, Y.M., Wimmer-Schweingruber, R.F., Aellig, M.R., Bochsler, P., Hefti, S., Mikić, Z.: 1999, The solar origin of corotating interaction regions and their formation in the inner heliosphere. *Space Sci. Rev.* **89**, 141. DOI.

Berger, T., Matthiä, D., Burmeister, S., Rios, R., Lee, K., Semones, E., Hassler, D.M., Stoffle, N., Zeitlin, C.: 2018, The solar particle event on 10 September 2017 as observed onboard the International Space Station (ISS). *Space Weather* **16**, 1173. DOI.

Bruno, A., Christian, E.R., de Nolfo, G.A., Richardson, I.G., Ryan, J.M.: 2019, Spectral analysis of the September 2017 solar energetic particle events. *Space Weather* **17**, 419. DOI.

Burlaga, L.F., Ness, N.F., Mariani, F., Bavassano, B., Villante, U., Rosenbauer, H., Schwenn, R., Harvey, J.: 1978, Magnetic fields and flows between 1 and 0.3 AU during the primary mission of Helios 1. *J. Geophys. Res.* **83**, 5167. DOI.

Burlaga, L.F., Sittler, E., Mariani, F., Schwenn, R.: 1981, Magnetic loop behind an interplanetary shock: Voyager, Helios, and IMP 8 observations. *J. Geophys. Res.* **86**, 6673. DOI.

Burton, R.K., McPherron, R.L., Russell, C.T.: 1975, An empirical relationship between interplanetary conditions and Dst. *J. Geophys. Res.* **80**, 4204. DOI.

Chamberlin, P.C., Woods, T.N., Didkovsky, L., Eparvier, F.G., Jones, A.R., Machol, J.L., Mason, J.P., Snow, M., Thiemann, E.M.B., Viereck, R.A., Woodraska, D.L.: 2018, Solar ultraviolet irradiance observations of the solar flares during the intense September 2017 storm period. *Space Weather* **16**, 1470. DOI.

Chapman, S., Ferraro, V.C.A.: 1931, A new theory of magnetic storms. *Terr. Magn. Atmos. Electr.* **36**, 77. DOI.

Chertok, I.M., Belov, A.V., Abunin, A.A.: 2018, Solar eruptions, forbush decreases, and geomagnetic disturbances from outstanding active region 12673. *Space Weather* **16**, 1549. DOI.

Crooker, N.U., Feynman, J., Gosling, J.T.: 1977, On the high correlation between long-term averages of solar wind speed and geomagnetic activity. *J. Geophys. Res.* **82**, 1933. DOI.

Davis, J.C.: 2002, *Statistics and Data Analysis in Geology*, Wiley, Hoboken. ISBN 9780471172758.

Davis, T.N., Sugiura, M.: 1966, Auroral electrojet activity index ae and its universal time variations. *J. Geophys. Res.* **71**, 785. DOI.

Dungey, J.W.: 1961, Interplanetary magnetic field and the auroral zones. *Phys. Rev. Lett.* **6**, 47. DOI.

Echer, E., Gonzalez, W.D., Tsurutani, B.T.: 2008, Interplanetary conditions leading to superintense geomagnetic storms (Dst ≤ -250 nT) during solar cycle 23. *Geophys. Res. Lett.* **35**, L06S03. DOI.

Finch, I.D., Lockwood, M.L., Rouillard, A.P.: 2008, Effects of solar wind magnetosphere coupling recorded at different geomagnetic latitudes: Separation of directly-driven and storage/release systems. *Geophys. Res. Lett.* **35**, L21105. DOI.

Gjerloev, J.W.: 2009, A global ground-based magnetometer initiative. *Eos Trans. AGU* **90**, 230. DOI.

Gonzalez, W.D., Joselyn, J.A., Kamide, Y., Kroehl, H.W., Rostoker, G., Tsurutani, B.T., Vasyliunas, V.M.: 1994, What is a geomagnetic storm? *J. Geophys. Res.* **99**, 5771. DOI.

Hajra, R., Tsurutani, B.T., Lakhina, G.S.: 2020, The complex space weather events of 2017 September. *Astrophys. J.* **899**, 3. DOI.

Hajra, R., Echer, E., Tsurutani, B.T., Gonzalez, W.D.: 2013, Solar cycle dependence of high-intensity long-duration continuous AE activity (HILDCAA) events, relativistic electron predictors? *J. Geophys. Res.* **118**, 5626. DOI.

Hajra, R., Tsurutani, B.T., Echer, E., Gonzalez, W.D.: 2014, Relativistic electron acceleration during high-intensity, long-duration, continuous AE activity (HILDCAA) events: Solar cycle phase dependences. *Geophys. Res. Lett.* **41**, 1876. DOI.

Hajra, R., Tsurutani, B.T., Echer, E., Gonzalez, W.D., Gjerloev, J.W.: 2016, Supersubstorms (SML < -2500 nT): Magnetic storm and solar cycle dependences. *J. Geophys. Res.* **121**, 7805. DOI.

Illing, R.M.E., Hundhausen, A.J.: 1986, Disruption of a coronal streamer by an eruptive prominence and coronal mass ejection. *J. Geophys. Res.* **91**, 10951. DOI.

Iyemori, T., Takeda, M., Nose, M., Odagi, Y., Toh, H.: 2010, Mid-latitude geomagnetic indices ASY and SYM for 2009 (provisional), internal report of data analysis center for geomagnetism and space magnetism. wdc.kugi.kyoto-u.ac.jp/aeasy/asy.pdf.

Jiggens, P., Clavie, C., Evans, H., O'Brien, T.P., Witasse, O., Mishev, A.L., Nieminen, P., Daly, E., Kalegaev, V., Vlasova, N., Borisov, S., Benck, S., Poivey, C., Cyamukungu, M., Mazur, J., Heynderickx, D., Sandberg, I., Berger, T., Usoskin, I.G., Paassilta, M., Vainio, R., Straube, U., Müller, D., Sánchez-Cano, B.,

Hassler, D., Praks, J., Niemelä, P., Leppinen, H., Punkkinen, A., Aminalragia-Giamini, S., Nagatsuma, T.: 2019, In situ data and effect correlation during September 2017 solar particle event. *Space Weather* **17**, 99. DOI.

Kennel, C.F., Edmiston, J.P., Hada, T.: 1985, *A Quarter Century of Collisionless Shock Research*, Am. Geophys. Un., Washington, 1. ISBN 9781118664032. DOI.

Klein, L.W., Burlaga, L.F.: 1982, Interplanetary magnetic clouds at 1 AU. *J. Geophys. Res.* **87**, 613. DOI.

Lepri, S.T., Zurbuchen, T.H.: 2010, Direct observational evidence of filament material within interplanetary coronal mass ejections. *Astrophys. J.* **723**, L22. DOI.

Matthiä, D., Meier, M.M., Berger, T.: 2018, The solar particle event on 10–13 September 2017: Spectral reconstruction and calculation of the radiation exposure in aviation and space. *Space Weather* **16**, 977. DOI.

Meng, X., Tsurutani, B.T., Mannucci, A.J.: 2019, The solar and interplanetary causes of superstorms (minimum Dst ≤ -250 nT) during the space age. *J. Geophys. Res.* **124**, 3926. DOI.

Milan, S.E., Gosling, J.S., Hubert, B.: 2012, Relationship between interplanetary parameters and the magnetopause reconnection rate quantified from observations of the expanding polar cap. *J. Geophys. Res.* **117**, A03226. DOI.

Newell, P.T., Gjerloev, J.W.: 2011, Evaluation of supermag auroral electrojet indices as indicators of substorms and auroral power. *J. Geophys. Res.* **116**, A12211. DOI.

Nykyri, K., Bengtson, M., Angelopoulos, V., Nishimura, Y., Wing, S.: 2019, Can enhanced flux loading by high-speed jets lead to a substorm? Multipoint detection of the Christmas day substorm onset at 08:17 UT, 2015. *J. Geophys. Res.* **124**, 4314. DOI.

O'Brien, T.P., Mazur, J.E., Looper, M.D.: 2018, Solar energetic proton access to the magnetosphere during the 10–14 September 2017 particle event. *Space Weather* **16**, 2022. DOI.

Ohtani, S.: 2001, Substorm trigger processes in the magnetotail: Recent observations and outstanding issues. *Space Sci. Rev.* **95**, 347. DOI.

Perreault, P., Akasofu, S.-I.: 1978, A study of geomagnetic storms. *Geophys. J. Roy. Astron. Soc.* **54**, 547. DOI.

Piersanti, M., Di Matteo, S., Carter, B.A., Currie, J., D'Angelo, G.: 2019, Geoelectric field evaluation during the September 2017 geomagnetic storm: MA.I.GIC. model. *Space Weather* **17**, 1241. DOI.

Pizzo, V.J.: 1985, *Interplanetary Shocks on the Large Scale: A Retrospective on the Last Decade's Theoretical Efforts*, Am. Geophys. Un., Washington, 51. ISBN 9781118664179. DOI.

Redmon, R.J., Seaton, D.B., Steenburgh, R., He, J., Rodriguez, J.V.: 2018, September 2017's geoeffective space weather and impacts to Caribbean radio communications during hurricane response. *Space Weather* **16**, 1190. DOI.

Richardson, I.G.: 2018, Solar wind stream interaction regions throughout the heliosphere. *Liv. Rev. Solar Phys.* **15**, 1. DOI.

Schillings, A., Nilsson, H., Slapak, R., Wintoft, P., Yamauchi, M., Wik, M., Dandouras, I., Carr, C.M.: 2018, O^+ escape during the extreme space weather event of 4–10 September 2017. *Space Weather* **16**, 1363. DOI.

Scolini, C., Chané, E., Temmer, M., Kilpua, E.K.J., Dissauer, K., Veronig, A.M., Palmerio, E., Pomoell, J., Dumbović, M., Guo, J., Rodriguez, L., Poedts, S.: 2020, CME–CME interactions as sources of CME geoeffectiveness: The formation of the complex ejecta and intense geomagnetic storm in 2017 early September. *Astrophys. J. Suppl.* **247**, 21. DOI.

Sheeley, N.R., Harvey, J.W.: 1981, Coronal holes, solar wind streams, and geomagnetic disturbances during 1978 and 1979. *Solar Phys.* **70**, 237. DOI.

Shue, J.-H., Chao, J.-K.: 2013, The role of enhanced thermal pressure in the earthward motion of the Earth's magnetopause. *J. Geophys. Res.* **118**, 3017. DOI.

Smith, E.J., Wolfe, J.H.: 1976, Observations of interaction regions and corotating shocks between one and five AU: Pioneers 10 and 11. *Geophys. Res. Lett.* **3**, 137. DOI.

Student: 1908, Probable error of a correlation coefficient. *Biometrika* **6**, 302.

Tsurutani, B.T., Gonzalez, W.D.: 1987, The cause of high-intensity long-duration continuous AE activity (HILDCAAs): Interplanetary Alfvén wave trains. *Planet. Space Sci.* **35**, 405. DOI.

Tsurutani, B.T., Gonzalez, W.D.: 1997, *The Interplanetary Causes of Magnetic Storms: A Review*, Am. Geophys. Un., Washington, 77. ISBN 9781118664612. DOI.

Tsurutani, B.T., Hajra, R.: 2021, The interplanetary and magnetospheric causes of geomagnetically induced currents (GICs) > 10 A in the Mäntsälä Finland pipeline: 1999 through 2019. *J. Space Weather Space Clim.* DOI.

Tsurutani, B.T., Lin, R.P.: 1985, Acceleration of >47 keV ions and >2 keV electrons by interplanetary shocks at 1 AU. *J. Geophys. Res.* **90**, 1. DOI.

Tsurutani, B.T., Meng, C.-I.: 1972, Interplanetary magnetic-field variations and substorm activity. *J. Geophys. Res.* **77**, 2964. DOI.

Tsurutani, B.T., Gonzalez, W.D., Tang, F., Akasofu, S.I., Smith, E.J.: 1988, Origin of interplanetary southward magnetic fields responsible for major magnetic storms near solar maximum (1978–1979). *J. Geophys. Res.* **93**, 8519. DOI.

Tsurutani, B.T., Gonzalez, W.D., Tang, F., Lee, Y.T.: 1992, Great magnetic storms. *Geophys. Res. Lett.* **19**, 73. DOI.

Tsurutani, B.T., Gonzalez, W.D., Gonzalez, A.L.C., Tang, F., Arballo, J.K., Okada, M.: 1995, Interplanetary origin of geomagnetic activity in the declining phase of the solar cycle. *J. Geophys. Res.* **100**, 21717. DOI.

Tsurutani, B.T., Gonzalez, W.D., Gonzalez, A.L.C., Guarnieri, F.L., Gopalswamy, N., Grande, M., Kamide, Y., Kasahara, Y., Lu, G., Mann, I., McPherron, R., Soraas, F., Vasyliunas, V.: 2006, Corotating solar wind streams and recurrent geomagnetic activity: A review. *J. Geophys. Res.* **111**, A07S01. DOI.

Tsurutani, B.T., Hajra, R., Echer, E., Gjerloev, J.W.: 2015, Extremely intense (SML ≤ -2500 nT) substorms: Isolated events that are externally triggered? *Ann. Geophys.* **33**, 519. DOI.

Werner, A.L.E., Yordanova, E., Dimmock, A.P., Temmer, M.: 2019, Modeling the multiple CME interaction event on 6–9 September 2017 with WSA-ENLIL+Cone. *Space Weather* **17**, 357. DOI.

Yan, X.L., Wang, J.C., Pan, G.M., Kong, D.F., Xue, Z.K., Yang, L.H., Li, Q.L., Feng, X.S.: 2018, Successive X-class flares and coronal mass ejections driven by shearing motion and sunspot rotation in active region NOAA 12673. *Astrophys. J.* **856**, 79. DOI.

Zhang, J., Richardson, I.G., Webb, D.F., Gopalswamy, N., Huttunen, E., Kasper, J.C., Nitta, N.V., Poomvises, W., Thompson, B.J., Wu, C.-C., Yashiro, S., Zhukov, A.N.: 2007, Solar and interplanetary sources of major geomagnetic storms (Dst ≤ -100 nT) during 1996–2005. *J. Geophys. Res.* **112**, A10102. DOI.

Zou, P., Jiang, C., Feng, X., Zuo, P., Wang, Y., Wei, F.: 2019, A two-step magnetic reconnection in a confined X-class flare in solar active region 12673. *Astrophys. J.* **870**, 97. DOI.

Zurbuchen, T.H., Richardson, I.G.: 2006, In-situ solar wind and magnetic field signatures of interplanetary coronal mass ejections. *Space Sci. Rev.* **123**, 31. DOI.